Precipitation behaviour of Al–Zn–Mg–Cu alloy and diffraction analysis from η′ precipitates in four variants

Wenchao Yang [a,b], Shouxun Ji [b], Mingpu Wang [a], Zhou Li [a]

[a] School of Materials Science and Engineering, Central South University, Hunan, Changsha 410083, China
[b] Brunel Centre for Advanced Solidification Technology (BCAST), Brunel University, Uxbridge UB8 3PH, UK

ABSTRACT

Age hardening at 160 °C was performed in an Al–6.0 wt.%Zn–2.3 wt.%Mg–1.8 wt.%Cu–0.1 wt.%Zr alloy. It was found that metastable η′ phases played a very important role in controlling this behaviour. The alloy reached the 193 HV peak hardness aged for 6 h. Transmission electron microscopy was used to characterise the morphology of η′ phases as main strengthening precipitates, and then the high-resolution transmission electron microscopy, combining with Transition Matrix calculation, was used to analysis the orientations and electron diffraction patterns of η′ precipitates. It was found that the η′ phases in four variants had only three different zone axis: $[2\bar{4}23]_{\eta'}$, $[10\bar{1}0]_{\eta'}$ and $[\bar{2}4\bar{2}3]_{\eta'}$, parallel to the $[110]_{Al}$ direction of Al matrix when they were precipitated. By integrating the atomic coordinates, structure factors and double diffraction effect, a new diffraction patterns model under the $[110]_{Al}$ zone axis was established, which was good in agreement with the experimental result. Simultaneously, Moiré fringes analytical technique was also used to quantitatively verify the lattice parameters and orientation variants of η′ precipitates, and demonstrated that Moiré fringes with about 0.7 nm spacing were the results of the interaction between the $0004_{\eta'}/000\bar{4}_{\eta'}$ diffraction of η′ precipitates in variants 3/4 under the $[10\bar{1}0]_{\eta'}$ zone axis and the $1\bar{1}1_{Al}/1\bar{1}\bar{1}_{Al}$ of Al matrix under the $[110]_{Al}$ zone axis. Furthermore, the high-resolution transmission electron microscopy image simulation for Moiré fringes of η′ precipitates in the Al matrix presented a good match with the experimental result.

1. Introduction

As heat-treatable aluminium alloys, Al–Zn–Mg–Cu alloys are always used in the aerospace and automotive industry due to the high strength and low density [1]. It has been recognized that the metastable nano-particles precipitated from the matrix are critical for the precipitation strengthening [2–4]. The usual precipitation sequence of Al–Zn–Mg–Cu alloys is described as: supersaturated solid solution (SSSS) → GP zones → η′ phase → η phase. GP zones are generally formed during room temperature ageing or the early stages of artificial ageing. It is accepted that there are two types of GP zones, i.e., GPI and GPII [5]. GPI zones are fully coherent with the Al matrix, with internal ordering of Zn and Al or Mg on the $\{001\}_{Al}$ planes, GPII zones are believed as Zn-rich layers on $\{111\}_{Al}$ planes. Generally, GPI and GPII zones can serve as nucleation sites for the metastable η′ phase [2]. Metastable η′ phase, instead of

stable η phase ($MgZn_2$), is believed to be responsible for the peak hardening of Al–Zn–Mg–Cu alloys [6].

Undoubtedly, there must be an inseparable relationships between the mechanical properties and the metastable η′ phase. Therefore, the η′ phase is widely studied in composition and crystal structure. So far, there exist several models for the composition and crystal structure of η′ phase. Initially, Gjonnes and Simensen [7] proposed an orthorhombic structure for η′ phase with stoichiometry $MgZn_2$. However, by means of the X-ray diffraction, Auld and Cousland [8] deduced that the η′ phase actually had a hexagonal structure with an approximate composition $Mg_4Zn_{11}Al$. Further, Li et al. [9] investigated the η′ phase by using high-resolution transmission electron microscopy (HRTEM) technology and confirmed that η′ phase presented a hexagonal structure but with different atom coordinates and composition ($Mg_2Zn_{5-x}Al_{2+x}$), compared with Auld and Cousland model. In 2001, Wolverton [10] used the first-principles total energy calculations for three distinct models above and demonstrated that the Auld and Cousland model yielded reasonable energetic whereas the other models did not, further proposed a low-energy stoichiometry $Mg_4Zn_{13}Al_2$. Recently, based on the three-dimensional electron diffraction intensity data,

Kverneland et al. [11] proposed a new model for η' phase with space group P63/mmc and $Mg_2Zn_{5-x}Al_{2+x}$ composition ($x = 2$–4), named "Model II". Obviously, although the composition of η' phase remained controversial, its crystal structure was believed as a hexagonal structure with lattice parameters $a = 0.496$ nm and $c = 1.402$ nm [8–11], and it exhibited a well-defined crystallographic orientation relationships with the Al matrix as: $(10\bar{1}0)_{\eta'}//\{110\}_{Al}$; $(\bar{1}2\bar{1}0)_{\eta'}//\{112\}_{Al}$; $(0001)_{\eta'}//\{111\}_{Al}$. If considering four $\{111\}_{Al}$ planes in the Al matrix, the η' phase with hexagonal structure might be precipitated in the way of its $(0001)_{\eta'}$ plane along any one of four $\{111\}_{Al}$ planes. Therefore, there were four equivalent variants, giving a total of four possible orientations of η' precipitates, which had been listed in Table 1 [12]. Obviously, the understanding for orientation relationships of η' phase should be very meaningful in the materials research. However, up to now, limited information was found to analysis and calculate the electron diffraction patterns from η' phase. Although Kverneland et al. [11] studied the composite diffraction patterns from η' phase and Al matrix taken along different zone axis, his work ignored the existence of double diffraction and the affect from the structure factors. Therefore, the further detailed work is still necessary.

The aims of this investigation are to examine systematically the orientation relationships between η' phase and Al matrix on the basis of the structure–property relationships in the Al–Zn–Mg–Cu alloy and then to analysis the electron diffraction patterns from η' phase in four variants under the $[110]_{Al}$ zone axis based on the Transform Matrix calculation. Finally, a new diffraction patterns model with four orientations for η' phase is established under the $[110]_{Al}$ zone axis of Al matrix. Furthermore, Moiré fringes analytical technique and HRTEM simulation are used to quantitatively verify the lattice parameters and orientation variants of η' phase on the base of the Model II proposed by Kverneland et al. [11].

2. Experimental

The Al–6.0 wt.%Zn–2.3 wt.%Mg–1.8 wt.%Cu–0.1 wt.%Zr alloy was used in this research. Prior to the heat treatment, the alloy sheet was cut into small samples with $5 \times 20 \times 20$ mm in size. Then the samples were heated up to 470 °C and maintained at the temperature for 1 h to achieve a complete solution, followed by an immediate water quenching in a tank to room temperature (~20 °C). Then, the ageing treatment was performed at 160 °C to elaborate the relationships between property and microstructures.

Vickers hardness was measured at 2 kg load for 15 s using a HV-5 sclerometer. Five indentations were performed for each sample and the average value was taken as the measurement. Based on the hardening curve, typical specimens under the different ageing time were selected for the detailed transmission electron microscopy (TEM) and HRTEM examinations. The specimens for TEM were prepared by a standard electro-polishing procedure. The electrolytic solution was a mixture of nitric acid and methyl alcohol (2:8). The polishing was operated at 22 V from −20 °C to −30 °C. A JEOL-2100F HRTEM was used for the microstructural investigation. The commercial CrystalKitX software [13] was used to establish a super-cell structure model and the MacTempasX software [13] was used to calculate the structure factors and simulate the HRTEM image based on the super-cell structure.

3. Results and discussion

3.1. The hardening curve

Fig. 1 shows the typical hardening curve of experimental alloy aged at 160 °C. The shape of curve showed that the hardness of
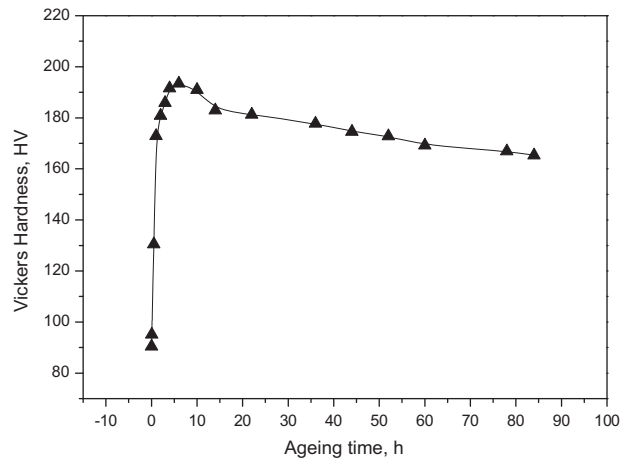
Table 1
Four equivalent orientation relationships between η' precipitates and Al matrix.

Variants	Orientation relationships
1	$(10\bar{1}0)_{\eta'}//(\bar{1}10)_{Al}$; $(\bar{1}2\bar{1}0)_{\eta'}//(\bar{1}\bar{1}2)_{Al}$; $(0001)_{\eta'}//(111)_{Al}$
2	$(10\bar{1}0)_{\eta'}//(\bar{1}10)_{Al}$; $(\bar{1}2\bar{1}0)_{\eta'}//(112)_{Al}$; $(0001)_{\eta'}//(11\bar{1})_{Al}$
3	$(10\bar{1}0)_{\eta'}//(110)_{Al}$; $(\bar{1}2\bar{1}0)_{\eta'}//(\bar{1}\bar{1}2)_{Al}$; $(0001)_{\eta'}//(\bar{1}11)_{Al}$
4	$(10\bar{1}0)_{\eta'}//(110)_{Al}$; $(\bar{1}2\bar{1}0)_{\eta'}//(112)_{Al}$; $(0001)_{\eta'}//(1\bar{1}1)_{Al}$

Fig. 1. Age-hardening curve of the experimental Al–Zn–Mg–Cu alloy aged at 160 °C.

alloy was increased sharply to the maximum value and followed by a decrease slowly. As seen in Fig. 1, the hardness was only 90.5 HV under the supersaturated solid solution state. It was rapidly increased to 193.5 HV at 6 h to reach the maximum hardness. With the further increase of ageing time, the hardness was gradually decreased to 165.3 HV at 84 h. Consequently, the specimens in under-aged (5 min and 3 h), peak-aged (6 h) and over-aged (78 h) states were selected for further detailed microstructural examinations.

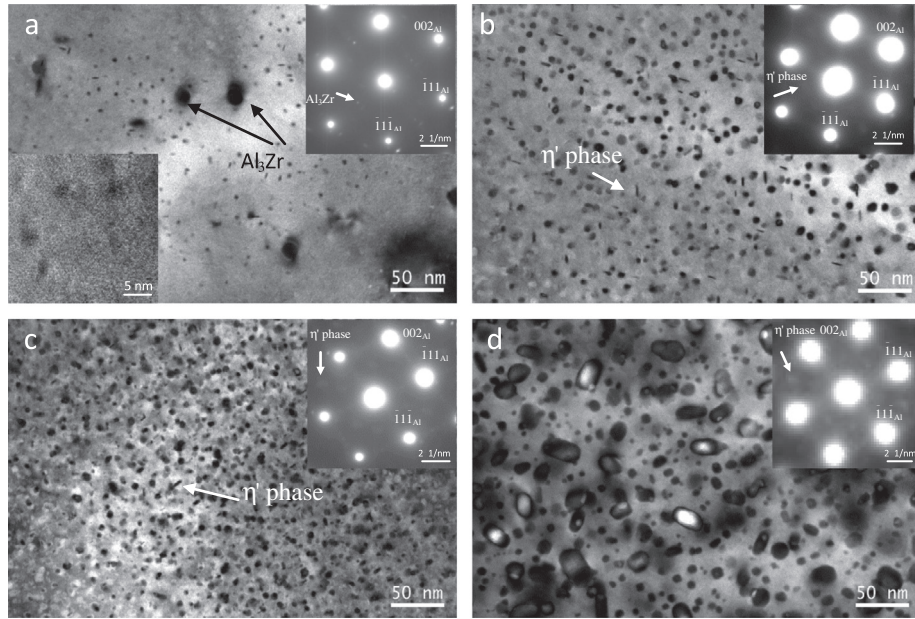### 3.2. Development of microstructures

Fig. 2 shows some bright-field (BF) TEM images and the corresponding select area diffraction patterns (SADP) of alloy aged at 160 °C for different times. In the early stage of ageing for 5 min, as shown in Fig. 2a, in addition to Al_3Zr particles with a size of 20 nm, a few precipitates had been formed in the Al matrix. The number density of these precipitates could be measured as $2.93 \times 10^3/\mu m^2$. It could be seen that most of precipitates displayed a round contrast, but some precipitates were slightly elongated along some directions. The HRTEM image, which was located at the lower left corner as an insert, showed that these precipitates were fully coherent with the Al matrix, and the size was less than 5 nm. From the corresponding SADP located at the upper right corner in Fig. 2a, some weak diffraction streaks could be observed apart from the diffraction spots of Al matrix and Al_3Zr particles (the diffraction spots of Al_3Zr particles were typically located at $1/2\,220_{Al}$ and $1/2\,200_{Al}$ diffraction positions [2]). It might indicate that GPI zones had formed at ageing for 5 min.

Upon further ageing to 3 h, although the samples were still in the under-aged stage (Fig. 1), the hardness had rapidly been raised to 185.9 HV (96.1% of the peak value). Compared with the result in Fig. 2a, a relative high density precipitates (about $8.96 \times 10^3/\mu m^2$) had been formed after ageing for 3 h in Fig. 2b. The sizes of precipitates were 10–20 nm. A few of precipitates had the short rod-shaped morphology and the others displayed the round morphology. It should be noted that these round precipitates might be the projections of the rod-shaped precipices under the different observation direction. These short rod-shaped precipitates were always believed to be η' precipitates in Refs. [14–16]. As seen from the SADP in Fig. 2b, the typical diffraction spots of η' precipitates were observed in addition to the diffraction spots from Al matrix.

Fig. 2c shows the microstructure of alloy in the peak hardness. It was clear that, although the number density of precipitates was increased rapidly to $29.6 \times 10^3/\mu m^2$, however, their sizes were basically maintained between 10 and 20 nm sizes. The clear

Fig. 2. Bright filed TEM images and the corresponding SADP of the experimental alloy aged at 160 °C for different stages. (a) 5 min, the HRTEM image was from the $[110]_{Al}$ zone axis, (b) 3 h, (c) 6 h and (d) 78 h. The SADPs were found as inserts in the upper right corner, and the diffraction spots from η′ phases were indicated by the arrows in the corresponding SADP.

diffraction spots in the SADP indicated that the η′ precipitates were still predominant in microstructure.

When the ageing time was prolonged to 78 h (over-aged stage), some precipitates were obviously coarsened, their maximum sizes had reached to 40–50 nm, as shown in Fig. 2d. Simultaneously, the number density of these precipitates was drastically decreased to $15.8 \times 10^3/\mu m^2$. However, the diffraction spots in the SADP under the $[110]_{Al}$ zone axis indicated that most of precipitates were still η′ phases in microstructure. The coarse and lower number density η′ phases did not effectively hinder the dislocation movement. Consequently, the hardness was decreased from the peak-value of 193.5 HV to a value of 165.3 HV at 78 h. Based on the microstructure observation above, it was obvious that η′ precipitates played a key role in controlling the hardening behaviour of experimental alloy. Therefore, it was necessary to analysis and characterise the precipitation behaviour of η′ phases in detail.

3.3. The morphology and orientation characterisation of η′ precipitates

Fig. 3 displays the enlarged BF TEM image from η′ precipitates and the corresponding SADP under the $[110]_{Al}$ zone axis. Under the $[110]_{Al}$ observation direction, two kinds of different morphologies could be seen in Fig. 3a: one was in the rod-shaped morphology and the other was in the round-shaped morphology, as indicated by the arrows. The rod-shaped η′ phases were 10 nm long and 2.5 nm wide, which were precipitated along the $(1\bar{1}\bar{1})_{Al}$ plane and $(1\bar{1}1)_{Al}$ plane, respectively. The round-shaped η′ phases were 5–10 nm in diameter, which might be precipitated along the other two $\{111\}_{Al}$ planes. Because there was a 35.26° between $(110)_{Al}$ plane and $(111)_{Al}$ plane or $(11\bar{1})_{Al}$ plane, the precipitates with on rod-shaped morphology were inevitably displayed under the $[110]_{Al}$ observation direction. The corresponding SADP from η′ phases was displayed in Fig. 3b. It should be noted that this
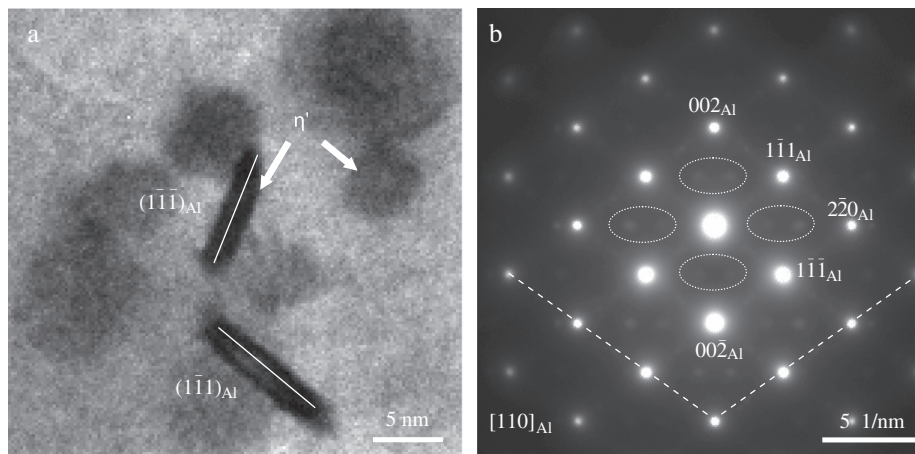
Fig. 3. Enlarged BF TEM images (a) of η′ precipitates along two different $\{111\}_{Al}$ planes and the corresponding SADP (b) under the $[110]_{Al}$ zone axis. The white arrows in (a) indicated two different morphologies of η′ precipitates. Some white ellipses and dotted lines in (b) represented the diffraction effect from η′ precipitates.

SADP contained some typical diffraction patterns and diffraction streaks from η′ phases, which were indicated by the white ellipses and dotted lines in Fig. 3b. These diffraction patterns were located at the 1/3 $2\bar{2}0_{Al}$ and 2/3 $2\bar{2}0_{Al}$ diffraction positions of Al matrix. On the other hand, the diffraction streaks presented two linear distributions: one was from $2\bar{2}0_{Al}$ diffraction spot to 002_{Al} diffraction spot; the other was from $00\bar{2}_{Al}$ diffraction spot to $2\bar{2}0_{Al}$ diffraction spot. Generally, the precipitates with certain orientation relationships often present some regular diffraction spots, which meet the parallelogram law in the SADP, such as S phases and θ′ phases precipitated from Al–Cu–Mg alloys and Al–Li–Cu alloys, respectively [17,18]. It was interesting that these diffraction patterns from η′ phases did not meet the parallelogram law, however, this kind of diffraction information was frequently found in Al–Zn–Mg–Cu series alloy to reflect the orientation of η′ phases.

As mentioned above, the η′ phases actually had four variants along four different $\{111\}_{Al}$ planes. Fig. 4 displays the HRTEM images of two η′ variants under the $[110]_{Al}$ zone axis, the corresponding Fast Fourier Transformation patterns (FFT) were displays as inserts in Fig. 4a and b, respectively. It was disappointing that no any clear periodical lattice fringes could be observed in two HRTEM images of η′ phases. Contrarily, some Moiré fringes were clearly observed. The spacing was measured about 0.7 nm in Fig. 4a and b. Together with the diffraction streaks in FFT patterns, undoubtedly, some double diffraction effect had inevitably happened between the η′ phase and the Al matrix. Therefore, this SADP from η′ phases in Fig. 3b should actually be complicated mixing electron diffraction patterns containing the double diffraction effect.

For a complicated mixing electron diffraction patterns, Transition Matrix can be used as a very useful tool in analysing it, which has been successfully applied in SADP from β″, β′ and Q′ precipitates with 12 variants in Al–Mg–Si alloys [19–21]. Generally, three sets of parallel crystal planes are first needed to establish the Transition Matrix. Let $(H_1K_1L_1)//(h_1k_1l_1)$, $(H_2K_2L_2)//(h_2k_2l_2)$ and $(H_3K_3L_3)//(h_3k_3l_3)$ be three sets of parallel crystal planes for η′ precipitate and Al matrix, respectively. Then, Transition Matrix $M(d)$ between the $[UVW]_{η′}$ and $[uvw]_{Al}$ directions can be described as follows:

$$\begin{bmatrix} U \\ V \\ W \end{bmatrix} = M(d) \begin{bmatrix} u \\ v \\ w \end{bmatrix} \tag{1}$$

$$M(d) = \begin{bmatrix} H_1 & K_1 & L_1 \\ H_2 & K_2 & L_2 \\ H_3 & K_3 & L_3 \end{bmatrix}^{-1} \begin{bmatrix} \frac{d_1}{D_1} & 0 & 0 \\ 0 & \frac{d_2}{D_2} & 0 \\ 0 & 0 & \frac{d_3}{D_3} \end{bmatrix} \begin{bmatrix} h_1 & k_1 & l_1 \\ h_2 & k_2 & l_2 \\ h_3 & k_3 & l_3 \end{bmatrix} \tag{2}$$

where D_i and d_i ($i = 1–3$) are the interplanear spacing of $\{H_iK_iL_i\}_{η′}$ and $\{h_ik_il_i\}_{Al}$, respectively. Furthermore, Transition Matrix between the $(HKL)_{η′}$ and $(hkl)_{Al}$ planes can be expressed as:

$$\begin{bmatrix} H \\ K \\ L \end{bmatrix} = M(p) \begin{bmatrix} h \\ k \\ l \end{bmatrix} \tag{3}$$

and

$$M(p) = \left[M(d)^T \right]^{-1} \tag{4}$$

That is, $M(p)$ is the inverse of Transpose Matrix of $M(d)$. Then, the direction $[UVW]$ and plane (HKL) of η′ phase, which are parallel to a given zone axis $[uvw]$ and corresponding crystal plane (hkl) of Al matrix, can be calculated easily. More detailed process about Transition Matrix calculation may refer to the reference [19]. Table 1 lists all of the orientation relationships from η′ phases in four variants. Based on the results in Table 1 and Transition Matrix calculation using formulas (1)–(4), all of the orientation relationships could be transformed in the given $[110]_{Al}$ zone axis. All of the Transition Matrix $M(d)$ and $M(p)$ values for four variants of η′ phases using for the orientation analysis and the corresponding orientation relationships could be deduced to list in Table 2. As seen in Table 2, the η′ phases had actually only three zone axis: $[2\bar{4}23]_{η′}$, $[10\bar{1}0]_{η′}$ and $[\bar{2}4\bar{2}3]_{η′}$, parallel to the $[110]_{Al}$ zone axis when they were precipitated from the Al matrix.

Furthermore, the simulated diffraction patterns of four η′ variants under different zone axis were displayed in Fig. 5, which was observed along the $[110]_{Al}$ direction of Al matrix. Fig. 5a–d displays the diffraction patterns under the $[2\bar{4}23]_{η′}$ $[\bar{2}4\bar{2}3]_{η′}$ and $[10\bar{1}0]_{η′}$ zone axis from variants 1–4, respectively. It should be noted that, although variants 1 and 2 had different zone axis, their diffraction patterns displayed the same shape; and although variants 3 and 4 had same zone axis, their diffraction patterns had a 70.53° angle. By overlapping the four simulated diffraction patterns of η′ phases with the $[110]_{Al}$ diffraction patterns of Al matrix, a model of mixing SADP under the given $[110]_{Al}$ zone axis could be obtained as shown in Fig. 5e, where the black line

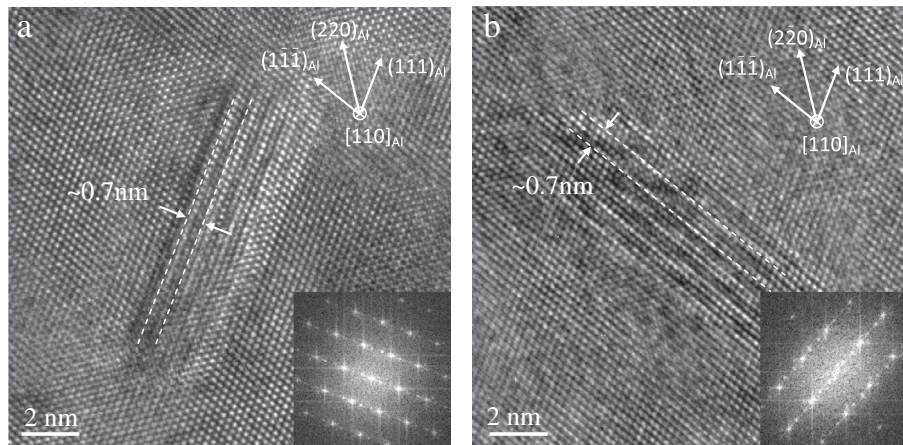**Fig. 4.** HRTEM images from two variants of η′ phases under the $[110]_{Al}$ zone axis, which were lying on the $(1\bar{1}1)_{Al}$ plane (a) and $(1\bar{1}\bar{1})_{Al}$ plane (b), respectively. The corresponding FFT patterns could be found as inserts. The spacing of Moiré fringes in HRTEM images was measured as about 0.7 nm.

Table 2

Transition Matrix $M(d)$ and $M(p)$ of four variants of η′ precipitates, and the corresponding orientation relationships based on the Transition Matrix calculation under the given $[110]_{Al}$ zone axis.

Variants	$M(d)$			$M(p)$			The corresponding orientation relationships under the given $[110]_{Al}$ zone axis
1	−2/3	2/3	0	−1/2	1	−1/2	$[2\bar{4}23]_{η'}//[110]_{Al}$; $(\bar{3}030)_{η'}//(2\bar{2}0)_{Al}$
	−2/3	0	2/3	−1/2	−1/2	1	
	1/6	1/6	1/6	2	2	2	
2	2/3	2/3	0	1	1/2	1/2	$[\bar{2}4\bar{2}3]_{η'}//[110]_{Al}$; $(\bar{3}030)_{η'}//(2\bar{2}0)_{Al}$
	−2/3	2/3	0	−1	1/2	−1/2	
	0	2/3	2/3	1/2	1/2	1	
3	2/3	2/3	0	1	1/2	1/2	$[10\bar{1}0]_{η'}//[110]_{Al}$; $(1\bar{2}1\bar{8})_{η'}//(2\bar{2}0)_{Al}$
	0	2/3	−2/3	−1/2	1/2	−1	
	−1/6	1/6	1/6	−2	2	2	
4	1/6	1/6	−1/6	2	2	−2	$[10\bar{1}0]_{η'}//[110]_{Al}$; $(1\bar{2}1\bar{8})_{η'}//(2\bar{2}0)_{Al}$
	0	2/3	2/3	−1/2	1/2	1	
	1/6	−1/6	1/6	2	−2	2	
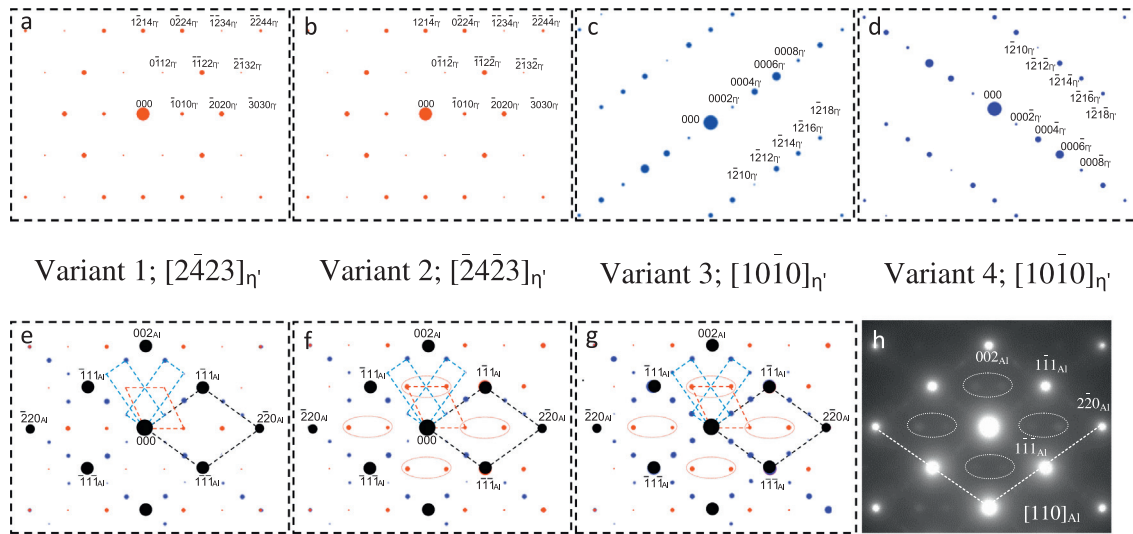
Fig. 5. Simulated diffraction patterns from four η′ variants based on the Transition Matrix calculation results. (a) $[2\bar{4}23]_{η'}$, (b) $[\bar{2}4\bar{2}3]_{η'}$, (c) $[10\bar{1}0]_{η'}$, (d) $[10\bar{1}0]_{η'}$ with 70.53° angle from (c and e) the overlapped diffraction patterns under the $[110]_{Al}$ zone axis, (f and g) the diffraction patterns after considering the double diffraction under the $[2\bar{4}23]_{η'}$, $[\bar{2}4\bar{2}3]_{η'}$ and the $[10\bar{1}0]_{η'}$ zone axis, respectively, and (h) comparison of the simulated $[110]_{Al}$ diffraction patterns and the experimental diffraction patterns. The black, red and blue lines displayed the periodic reciprocal lattice of Al matrix, variants 1/2, variants 3 and 4, respectively. (For interpretation of the references to colour in this figure legend, the reader is referred to the web version of this article.)

Table 3

Spacings of the Moiré fringes for η′ precipitate and Al matrix. The lattice parameters a = 0.496 nm, c = 1.402 nm and $γ$ = 120° for η′ precipitate and a = 0.405 nm for Al matrix are used for calculations. And, the orientation relationships in bold will be used for the quantitative Moiré fringes simulation in Fig. 6.

Variants	Zone axis	Set of g vectors	Corresponding plane spacing (nm)	Spacing of moiré fringes (nm)
1(2)	$[2\bar{4}23]_{η'}//[110]_{Al}$	$1\bar{2}14_{η'}/002_{Al}$	$d_{1\bar{2}14\,η'}$ = 0.203; $d_{002\,Al}$ = 0.203	∞
		$\bar{2}020_{η'}/2\bar{2}0_{Al}$	$d_{2020\,η'}$ = 0.215; $d_{220\,Al}$ = 0.143	0.427
		$\bar{1}\bar{1}22_{η'}/1\bar{1}1_{Al}$	$d_{\bar{1}\bar{1}22\,η'}$ = 0.234; $d_{1\bar{1}1\,Al}$ = 0.234	∞
3(4)	$[10\bar{1}0]_{η'}//[110]_{Al}$	$1\bar{2}12_{η'}/1\bar{1}\bar{1}_{Al}$	$d_{1\bar{2}12\,η'}$ = 0.234; $d_{1\bar{1}\bar{1}\,Al}$ = 0.234	∞
		$0004_{η'}/1\bar{1}1_{Al}$	$d_{0004\,η'}$ = 0.351; $d_{1\bar{1}1\,Al}$ = 0.234	0.702
		$0006_{η'}/1\bar{1}1_{Al}$	$d_{0006\,η'}$ = 0.234; $d_{1\bar{1}1\,Al}$ = 0.234	∞

displayed the periodic diffraction patterns from Al matrix, the red line outlined the periodic diffraction spots from variants 1 and 2, the blue lines represented the periodic diffraction spots from variants 3 and 4, respectively, It should be noted that the atom coordinates and structure factors of η′ phase with chemical formula-Mg₄Zn₁₃Al₂ had been considered during the simulation process based on the Model II proposed by Kverneland. However, it was also obvious that the diffraction patterns model in Fig. 5e was not exactly consistent with the experimental result (Fig. 4b), e.g. these diffraction spots located at the 1/3 $2\bar{2}0_{Al}$ and 2/3 $2\bar{2}0_{Al}$ diffraction positions in Fig. 5e presents the different diffraction

intensity. Based on the HRTEM observation in Fig. 4, the double diffraction effect was actually inevitable resulting from some Moiré fringes. Therefore, the double diffraction effect needed to be considered in the simulation process. Fig. 5f and g shows two new simulation diffraction patterns. In Fig. 5f, the double diffraction effect under the $[2\bar{4}23]_{η'}$ and $[\bar{2}4\bar{2}3]_{η'}$ directions were considered. It was found that these characteristic diffraction spots located at the 1/3 $2\bar{2}0_{Al}$ and 2/3 $2\bar{2}0_{Al}$ diffraction positions displayed basically same diffraction intensity. In Fig. 5g, the double diffraction effect under the $[10\bar{1}0]_{η'}$ direction was considered. It was clear that the diffraction streaks from $2\bar{2}0_{Al}/\bar{2}20_{Al}$ to 002_{Al}

Table 4
Structure factors of different crystal planes of η′ precipitate in Model II [11]. The three strongest diffractions in bold were selected for Moiré fringes calculations, respectively.

Plane index ($[2\bar{4}23]_{\eta'}$ zone axis)	$\bar{1}010$	$\bar{2}020$	$\bar{3}030$	$\bar{2}1\bar{3}2$	$\bar{1}1\bar{2}2$	$0\bar{1}12$	$\bar{2}\bar{2}44$	$\bar{1}\bar{2}34$	$0\bar{2}24$	$\bar{1}\bar{2}14$
Structure factors	8.36	**22.79**	0.28	0.63	**14.43**	0.7	6.78	1.06	10.11	**11.16**
Plane index ($[10\bar{1}0]_{\eta'}$ zone axis)	$000\bar{2}$	$000\bar{4}$	$000\bar{6}$	$000\bar{8}$	$1\bar{2}18$	$1\bar{2}16$	$1\bar{2}1\bar{4}$	$1\bar{2}1\bar{2}$	$1\bar{2}10$	$1\bar{2}14$
Structure factors	2.72	**18.61**	**32.70**	5.65	0.16	6.13	11.16	**14.43**	0.99	11.16
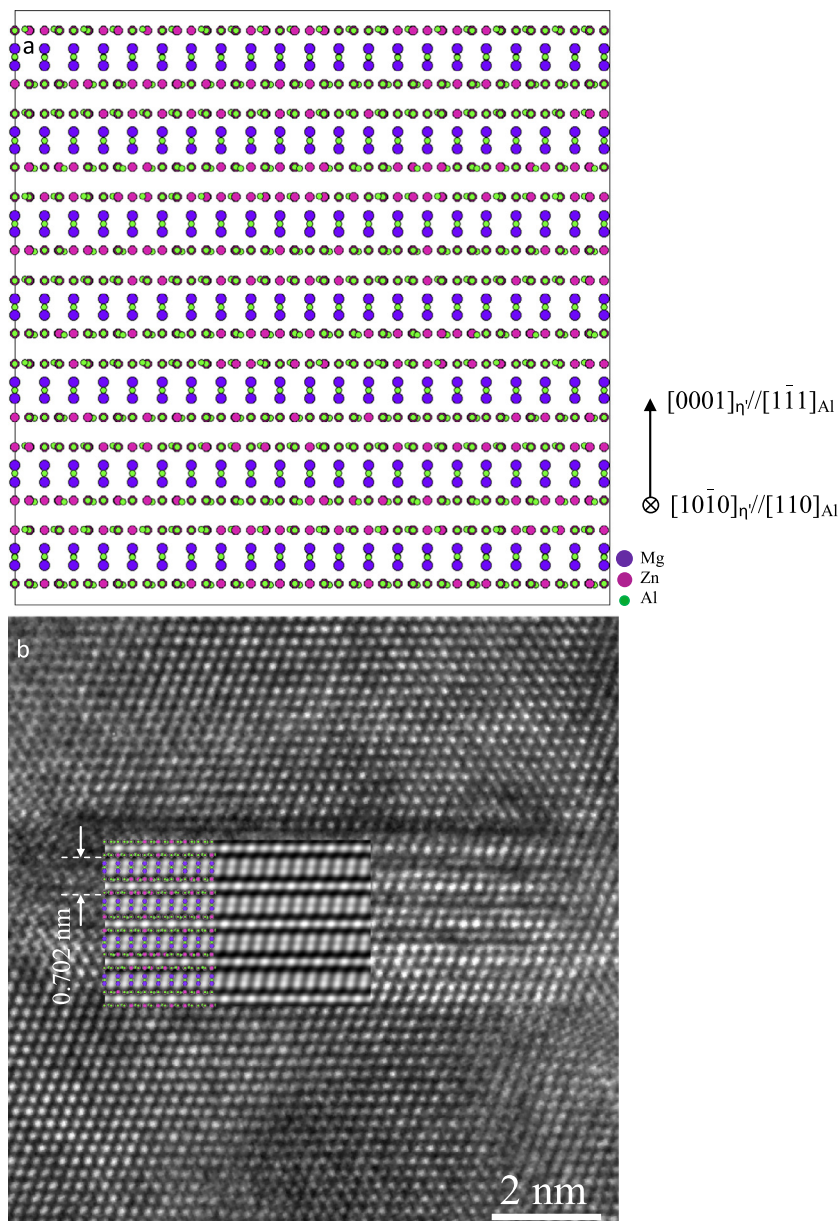
Fig. 6. (a) η′ Phase/Al matrix overlapped model created using the orientation relationships (bold-type) in Table 3, viewed along a $[1\,1\,0]_{Al}$ direction, (b) experimental HRTEM image with a superimposed Moiré fringes simulation image according to the model in (a), the insert was a simulated Moiré fringes at thickness $t = 4$ nm and defocus $\Delta f = -50$ nm.

diffraction spots were confirmed. Finally, Fig. 5h gave the comparison of the simulated $[1\,1\,0]_{Al}$ diffraction patterns and the experimental diffraction patterns. It was found that the simulation diffraction patterns was in excellent agreement with the experimental SADP.

3.4. Moiré fringes analysis and simulation of η′ phase in Al matrix

The Moiré fringes from η′ phase could always be found in HREM images as shown in Fig. 4. Generally, the reason of Moiré fringes formation is that a stronger diffraction beam from the upper crystal will become the incident beam of the following crystal to produce the double diffraction effect. The spacing of Moiré fringes formed by diffraction vectors g_1 and g_2 is given as $1/|\Delta g|$, and the direction of the fringes is normal to the Δg direction. Here, $\Delta g = g_1 - g_2$. Based on the diffraction information of η′ phase in Fig. 5, therefore, the spacing of the Moiré fringes could be described quantitatively by reference to Table 3.

The structure factors of different diffraction planes were calculated by the MacTempasX software based on the Model II, the

results were listed in Table 4. Three strongest diffractions were selected for Moiré fringes calculations: $\bar{2}020_{\eta'}$ (22.79), $\bar{1}\bar{1}22_{\eta'}$ (14.43) and $1\bar{2}14_{\eta'}$ (11.16) diffractions under the $[2\bar{4}23]_{\eta'}$ zone axis (please note: the diffraction information were the same under the $[2\bar{4}23]_{\eta'}$ and $[\bar{2}4\bar{2}3]_{\eta'}$ zone axis), and $000\bar{6}_{\eta'}$ (32.70), $000\bar{4}_{\eta'}$ (18.61) and $1\bar{2}1\bar{2}_{\eta'}$ (14.43) diffraction under the $[10\bar{1}0]_{\eta'}$ zone axis. As seen in Table 3, $\bar{2}020_{\eta'}$ and $2\bar{2}0_{Al}$ diffractions would produce the Moiré fringes with 0.427 nm spacing, and $0004_{\eta'}$ and $1\bar{1}1_{Al}$ diffractions would form the Moiré fringes with 0.702 nm spacing. The remaining diffractions could not produce any visible Moiré fringes because their spacing was much larger than the size of η' precipitates. Therefore, according to results in Table 3, it could be known that the Moiré fringes with about 0.7 nm spacing in Fig. 4 should be the results of the interaction between the $0004_{\eta'}/000\bar{4}_{\eta'}$ diffraction of η' precipitates in variants 3/4 under the $[10\bar{1}0]_{\eta'}$ zone axis and $1\bar{1}1_{Al}/1\bar{1}\bar{1}_{Al}$ diffraction of the Al matrix under the $[110]_{Al}$ zone axis.

Further, an overlapped atomic model of η' phase/Al matrix was constructed using CrystalKit software based on the orientation relationships (bold-type) in Table 3. The result was shown in Fig. 6a, viewed along a $[110]_{Al}$ direction. And then, the atomic model was input into the MacTempas multi-slice programs to perform HRTEM image simulation. The simulated HRTEM result for a specimen thickness $t = 4$ nm and defocus $\Delta f = -50$ nm was shown as an insert in Fig. 6b, which clearly displayed some simulated Moiré fringes with 0.702 nm spacing. The simulated image provided a good match with the experimental image. Simultaneously, according to the evidences presented and quantitative Moiré fringes analysis, we further verified the lattice parameters and orientation variants of η' precipitates.

4. Conclusions

The precipitation behaviour of an Al–6.0 wt.%Zn–2.3 wt.%Mg–1.8 wt.%Cu–0.1 wt.%Zr alloy and the diffraction patterns from the metastable η' precipitates are investigated by HRTEM and Transition Matrix calculation. It is found that the alloy can reach 193 HV peak hardness from 90.4 HV at SSSS when it is aged for 6 h at 160 °C. Metastable η' phases play a very important role in controlling this behaviour. Furthermore, four orientations of η' precipitates with hexagonal crystal structure are analysed systematically under the $[110]_{Al}$ zone axis. Transition Matrix is used to analysis the complicated mixing electron diffraction patterns, and find that the η' phases have only three zone axis: $[2\bar{4}23]_{\eta'}$, $[10\bar{1}0]_{\eta'}$ and $[\bar{2}4\bar{2}3]_{\eta'}$, parallel to the $[110]_{Al}$ zone axis when they are precipitated from the Al matrix. Based on the Transition Matrix calculation, a new diffraction patterns model from η' precipitates

in four variants is established under the $[110]_{Al}$ zone axis. This model shows a good agreement with the experimental result. Simultaneously, Moiré fringes analytical technique is also used to quantitatively verify the lattice parameters and orientation variants of η' precipitates, and demonstrates that the Moiré fringes with about 0.7 nm spacing displayed in HRTEM image should be the results of the interaction between the $0004_{\eta'}/000\bar{4}_{\eta'}$ diffraction of η' recipitates in variants 3/4 under the $[10\bar{1}0]_{\eta'}$ zone axis and $1\bar{1}1_{Al}/1\bar{1}\bar{1}_{Al}$ diffraction of the Al matrix under the $[110]_{Al}$ zone axis. Furthermore, the HRTEM image simulation for Moiré fringes of η' precipitates in the Al matrix presents a good match with the experimental result.

References

[1] N. Kamp, I. Sinclair, M.J. Starink, Metall. Mater. Trans. A 33 (2002) 1125–1136.
[2] G. Sha, A. Cerezo, Acta Mater. 52 (2004) 4503–4516.
[3] T. Marlaud, A. Deschamps, F. Bely, W. Lefebvre, B. Baroux, Acta Mater. 58 (2010) 4814–4826.
[4] J. Buha, R.N. Lumley, A.G. Crosky, Mater. Sci. Eng., A 492 (2008) 1–10.
[5] L.K. Berg, J. Gjønnes, V. Hansen, X.Z. Li, M. Knutson-Wedel, G. Waterloo, D. Schryvers, L.R. Wallenberg, Acta Mater. 49 (2001) 3443–3451.
[6] J. Chen, L. Zhen, S. Yang, W. Shao, S. Dai, Mater. Sci. Eng., A 500 (2009) 34–42.
[7] J. Gjonnes, C.J. Simensen, Acta Mater. 18 (1970) 881–890.
[8] J.H. Auld, S.M. Cousland, Scr. Metall. 5 (1971) 765–769.
[9] X.Z. Li, V. Hansen, J. GjØnnes, L.R. Wallenberg, Acta Mater. 47 (1999) 2651–2659.
[10] C. Wolverton, Acta Mater. 49 (2001) 3129–3142.
[11] A. Kverneland, V. Hansen, R. Vincent, K. Gjønnes, Ultramicroscopy 106 (2006) 492–502.
[12] H. Yu, M. Wang, Y. Jia, Z. Xiao, C. Chen, Q. Lei, Z. Li, W. Chen, H. Zhang, Y. Wang, C. Cai, J. Alloys Comp. 601 (2014) 120–125.
[13] R. Kilaas. Total Resolution LLC. <http://www.totalresolution.com/contact.htm>.
[14] Y.Y. Li, L. Kovarik, P.J. Phillips, Y.F. Hsu, W.H. Wang, M.J. Mills, Phil. Mag. Lett. 92 (2012) 166–178.
[15] J.Z. Liu, J.H. Chen, X.B. Yang, S. Ren, C.L. Wu, H.Y. Xu, J. Zou, Scr. Mater. 63 (2010) 1061–1064.
[16] M. Dumont, W. Lefebvre, B. Doisneau-Cottignies, A. Deschamps, Acta Mater. 53 (2005) 2881–2892.
[17] S.C. Wang, M.J. Starink, Acta Mater. 55 (2007) 933–941.
[18] R. Yoshimura, T.J. Konno, E. Abe, K. Hiraga, Acta Mater. 51 (2003) 4251–4266.
[19] W. Yang, M. Wang, Y. Jia, R. Zhang, Metall. Mater. Trans. A 42 (2011) 2917–2929.
[20] W. Yang, M. Wang, X. Sheng, Q. Zhang, L. Huang, Philos. Mag. Lett. 91 (2011) 150–160.
[21] W. Yang, M. Wang, R. Zhang, Q. Zhang, X. Sheng, Scr. Mater. 62 (2010) 705–708.